International Journal of Solids and Structures 48 (2011) 1141–1153

Contents lists available at ScienceDirect

International Journal of Solids and Structures

journal homepage: www.elsevier.com/locate/ijsolstr

Elastic interaction of interfacial spherical-cap cracks in hollow particle filled composites

G. Tagliavia, M. Porfiri *, N. Gupta

Department of Mechanical and Aerospace Engineering, Polytechnic Institute of New York University, Six MetroTech Center, Brooklyn, NY 11201, USA

ARTICLE INFO

Article history:
Received 7 May 2010
Received in revised form 5 November 2010
Available online 30 December 2010

Keywords:
Crack shielding
Debonding
Interfacial crack
Multiple cracks
Strain energy release rate
Syntactic foams

ABSTRACT

This work analyzes the elastic interaction between two spherical-cap cracks present along the outer surface of a hollow particle embedded in a dissimilar medium under remote uniaxial tensile loading. A semi-analytical approach based on an enriched Galerkin method is adopted to determine stress and deformation fields as functions of particle wall thickness and cracks' configuration. The present analysis is limited to multiple interfacial spherical-cap cracks; that is, crack propagation is restrained to the particle-matrix interface and possibility of crack kinking in the matrix is not considered. Interfacial crack growth characteristics, conditions for stable crack propagation, equal crack growth, and shielding are established through energy release rate analysis. The study is relevant to the analysis of tensile and flexural failure of syntactic foams used in marine and aerospace applications. Results specialized to glass-vinyl ester syntactic foams demonstrate that particle wall thickness can be used to control crack stability and growth characteristics as well as tailoring the magnitude of the shielding phenomenon. Predictions are compared to finite element findings for validation and to results for penny-shaped cracks to elucidate the role of crack curvature.

1. Introduction

Syntactic foams are composite materials obtained by dispersing hollow particles in a matrix (Narkis et al., 1984) with the twofold intent of improving properties and reducing density of the matrix. Selection of constituent materials, particle volume fraction, and particle wall thickness allows for tailoring the composite properties (see for example Gupta et al., 2010; Islam and Kim, 2007; John et al., 2007). The presence of porosity enclosed inside thin inclusions improves dimensional stability by providing low moisture absorption and thermal expansion (see for example Rohatgi et al., 2006; Sauvant-Moynot et al., 2006).

Designing marine and aerospace load bearing structures requires a thorough understanding of structure-property correlations and failure mechanisms in syntactic foams. Polymer matrix syntactic foams have received great attention for their wide application spectrum (see for example Bardella and Genna, 2001a; Gladysz et al., 2006; Gupta et al., 2010). Experimental studies on compressive response of glass-vinyl ester and epoxy syntactic foams show that failure is largely due to particle crushing (Gupta et al., 2010; Kim and Plubrai, 2004) whereas the particle-matrix interface plays an important role in determining the failure mechanisms under tensile and flexural conditions (Gupta et al., 2010; Tagliavia et al., 2010a; Wouterson et al., 2005). Scanning electron micrographs of tensile fracture surfaces show interfacial failure and curvilinear deformation marks in the matrix (see for example Kishore et al., 2005; Koopman et al., 2006). Similar features are also found in solid particle filled composites (see for example Lee and Yee, 2001; Pawlak and Galeski, 2002).

Theoretical studies have elucidated the role of particle wall thickness and volume fraction on the elastic properties of syntactic foams by considering perfect bonding at the particle-matrix interface (see for example Bardella and Genna, 2001b; Huang and Gibson, 1993; Marur, 2005; Porfiri and Gupta, 2009). These studies are further extended to include compliant interfacial layers in Marur (2009); within this model, full contact is assumed to be present at the particle-matrix interface. This approach is not applicable to the analysis of interfacial cracks formed during debonding, which is the failure mechanism in syntactic foams under tensile and flexural loading. Such failures are analyzed in a recent work where the problem of a single partially debonded inclusion embedded in an infinite matrix and subjected to uniaxial tensile loading is studied (Tagliavia et al., 2010b). Therein, a computationally efficient approach based on an enriched Galerkin method is utilized to solve the set of governing integral equations. The method is similar to enriched finite element and meshless methods proposed in Ayhan et al. (2006), Ching and Batra (2001), Fleming et al. (1997), and Singh et al. (2010), where the basis set is enriched with special

* Corresponding author. Tel.: +1 718 260 3681; fax: +1 718 260 3532.
E-mail addresses: gtagli01@students.poly.edu (G. Tagliavia), mporfiri@poly.edu (M. Porfiri), ngupta@poly.edu (N. Gupta).

0020-7683/$ - see front matter © 2010 Elsevier Ltd. All rights reserved.
doi:10.1016/j.ijsolstr.2010.12.017

functions to capture singularities and oscillations of the stress fields in the proximity of crack tips. A parametric study is conducted to understand the effect of particle wall thickness and debonding extent on elastic compliance, energy release rate (ERR), stress and displacement distributions along the interface, fracture mode mixity, and crack kink angle. However, the analysis presented in Tagliavia et al. (2010b) is limited to two equal spherical-cap cracks symmetrically located with respect to the loading direction at the particle poles.

In the presernt work, the framework developed in Tagliavia et al. (2010b) is extended to the case of two dissimilar interfacial cracks with the goal of understanding stability, growth characteristics, and shielding of cracks in syntactic foams. Such extension allows for ascertaining stability of a system of cracks by characterizing the system energetics in response to crack surface perturbations. Moreover, crack growth characteristics are analyzed by studying a constrained optimization problem to determine conditions for individual and equal crack growths. Single and double interfacial crack scenarios are compared to understand crack shielding and amplification phenomena. An extensive parametric study is performed to elucidate the role of particle wall thickness and crack configurations in the elastic interaction of spherical-cap cracks along the particle-matrix interface. This study is applicable to syntactic foams with low particle volume fraction as it neglects particle-to-particle interactions and focuses on a single inclusion embedded in an infinite matrix. Results are verified through finite element analysis (FEA) and compared with findings for penny-shaped cracks (see for example Gorbatikh, 2004; Kilic and Madenci, 2007), which enables understanding the effect of the interfacial crack curvature on the ERR.

The paper is organized as follows. In Section 2, the problem under investigation is defined. In Section 3, the set of integral governing equations for the interfacial stress fields is derived. In Section 4, the adopted semi-analytical solution is described. In Section 5, fundamental concepts of crack energetics are introduced. Results on glass-vinyl ester systems are presented and discussed in Section 6. FEA validation, remarks on stability criteria, and comparison with the penny-shaped crack scenario are presented in Section 7. In Section 8, main findings from this study are summarized. A series solution of Navier–Cauchy equation from (Lur'e, 1964) and some required expressions from (Tagliavia et al., 2010b) are included in the Appendix.

2. Problem statement

The proposed model geometry consists of a single hollow spherical inclusion embedded in an infinitely extended matrix, see Fig. 1a. A remote uniaxial tensile loading σ_∞ is applied along the y-direction. A spherical coordinate system (r,θ,ϕ) is selected to describe displacement and stress fields that are identified using the notation in Lur'e (1964), see Section A.1 in the Appendix.

Particle geometry is defined by the outer radius a and the radius ratio η, which is the ratio between the inner and the outer radii. Two spherical-cap cracks preexist at the poles of the inclusion, see Fig. 1a. Cracks' extents are identified by the crack tip angles α_1 and α_2 measured from the y-axis, as shown in Fig. 1a. In addition, materials comprising the inclusion and the matrix are assumed to be homogeneous, isotropic, and linear elastic. Particle shape, crack geometry, constituents' material properties, and loading conditions allow the three-dimensional problem to be reduced to a two-dimensional (2D) one. In what follows, subscripts i and m refer to the inclusion and the matrix, respectively.

By using the superposition principle, the problem is partitioned into the three subproblems sketched in Fig. 1b. The subproblems are: (I) the matrix material with a spherical void of radius a under remote uniaxial tensile stress σ_∞; (II) the matrix material with a spherical void of radius a loaded by an unknown traction distribution represented by $\sigma(\theta)$ along the radial direction and $\tau(\theta)$ along the circumferential direction, such that $\sigma(\theta)=\tau(\theta)=0$ for $-\alpha_1 \leqslant \theta \leqslant \alpha_1$ and $\alpha_2 \leqslant \theta \leqslant 2\pi-\alpha_2$; and (III) a hollow inclusion loaded by $\sigma(\theta)$ and $\tau(\theta)$ at its outer surface. Since the problem under investigation is symmetric with respect to the y-direction, only the interval $[0,\pi]$ is considered in the analysis. In what follows, superscripts (I), (II), and (III) are used to identify the solution of the corresponding subproblem.

3. Governing equations

In each constituent, displacement and stress fields can be expressed in the general series form, reported in Appendix in equation set (A2), by specializing elastic constants to inclusion and matrix materials, respectively (Lur'e, 1964). By applying suitable boundary conditions to each subproblem, solutions for radial and circumferential displacements at the interface are obtained as functions of $\sigma(\theta)$ and $\tau(\theta)$. For convenience, these unknown fields are expressed in terms of solid spherical harmonics, that is,

$$\sigma(\theta)=\sum_{n=0}^{\infty}\sigma_n P_n(\cos\theta), \tag{1a}$$

$$\tau(\theta)=\sum_{n=1}^{\infty}\tau_n \frac{\mathrm{d}P_n(\cos\theta)}{\mathrm{d}\theta}. \tag{1b}$$

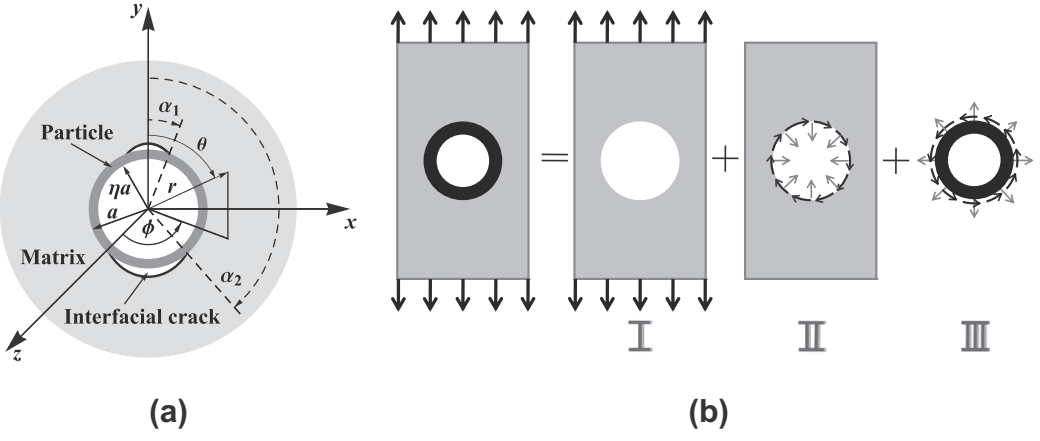

Fig. 1. (a) Schematic of model geometry containing two dissimilar interfacial cap cracks and (b) problem decomposition.

Here, $P_n(\cos\theta)$ is the nth Legendre polynomial as a function of $\cos\theta$ and the coefficients σ_n and τ_n are given by

$$\sigma_n = \frac{(2n+1)}{2}\int_{\alpha_1}^{\alpha_2}\sigma(\theta)P_n(\cos\theta)\sin\theta\mathrm{d}\theta, \tag{2a}$$

$$\tau_n = \frac{(2n+1)}{2n(n+1)}\int_{\alpha_1}^{\alpha_2}\tau(\theta)\frac{\mathrm{d}P_n(\cos\theta)}{\mathrm{d}\theta}\sin\theta\mathrm{d}\theta, \tag{2b}$$

due to the orthogonality of the Legendre polynomials and their derivative with respect to θ in $[0,\pi]$ and the fact that $\sigma(\theta)$ and $\tau(\theta)$ are zero for $0 \leqslant \theta \leqslant \alpha_1$ and $\alpha_2 \leqslant \theta \leqslant \pi$. Such unknown stress fields are determined by imposing the continuity of radial and circumferential displacements across the intact part of the interface ($\alpha_1 < \theta < \alpha_2$), that is,

$$u_r(a^+,\theta) - u_r(a^-,\theta) = u_r^{(\mathrm{I})}(a,\theta) + u_r^{(\mathrm{II})}(a,\theta) - u_r^{(\mathrm{III})}(a,\theta) = 0, \tag{3a}$$

$$u_\theta(a^+,\theta) - u_\theta(a^-,\theta) = u_\theta^{(\mathrm{I})}(a,\theta) + u_\theta^{(\mathrm{II})}(a,\theta) - u_\theta^{(\mathrm{III})}(a,\theta) = 0. \tag{3b}$$

Here, superscripts + and − are used to identify limits from the matrix and inclusion side, respectively. Solutions of subproblems (I) and (II) are derived in Tagliavia et al. (2010b) under the assumption of a symmetric crack configuration with respect to the xz-plane of the particle, namely, $\alpha_1 = \pi - \alpha_2$. As a consequence, only even terms in equation set (A2) are retained. Releasing this assumption requires keeping both even and odd terms in the series without altering the solution format. These expressions are not derived here again and are only reported in equation sets (A5) and (A6). In what follows, solution of subproblem (III) is treated in detail.

A solution for subproblem (III) exists if the external loading describes a self-equilibrated system of forces (Lur'e, 1964), that is,

$$2\pi a^2\int_0^\pi[\sigma(\theta)\cos\theta - \tau(\theta)\sin\theta]\sin\theta\mathrm{d}\theta = 0. \tag{4}$$

Substituting equation set (1) in Eq. (4) provides

$$\sigma_1 + 2\tau_1 = 0. \tag{5}$$

The solution for a hollow inclusion loaded by $\sigma(\theta)$ and $\tau(\theta)$ is written in the form of equation set (A2), where the elastic constants are specific to the inclusion material and the constants A_n, B_n, C_n, and D_n are determined by imposing

$$\sigma_{rr}^{(\mathrm{III})}(a,\theta) = \sigma(\theta), \tag{6a}$$

$$\tau_{r\theta}^{(\mathrm{III})}(a,\theta) = \tau(\theta), \tag{6b}$$

$$\sigma_{rr}^{(\mathrm{III})}(\eta a,\theta) = 0, \tag{6c}$$

$$\tau_{r\theta}^{(\mathrm{III})}(\eta a,\theta) = 0. \tag{6d}$$

Note that Eqs. (6c) and (6d) correspond to stress-free conditions on the inner surface of the inclusion.

The solution of equation set (6) is obtained by exploiting the orthogonality of the sets $\{P_n(\cos\theta)\}_{n=0}^\infty$ and $\{\mathrm{d}P_n(\cos\theta)/\mathrm{d}\theta\}_{n=0}^\infty$ in $[0,\pi]$. For $n \neq 1$, equation set (6) reduces to a linear system of four equations in four unknowns, where A_n, B_n, C_n, and D_n are given by

$$A_n = \frac{a^{-n}\left[\mathrm{C}_n^{(A\sigma)}\sigma_n + \mathrm{C}_n^{(A\tau)}\tau_n\right]}{2\mu_i\mathrm{D}_n^{(A)}}, \tag{7a}$$

$$B_n = -\frac{a^{2-n}\left[\mathrm{C}_n^{(B\sigma)}\sigma_n + \mathrm{C}_n^{(B\tau)}\tau_n\right]}{2\mu_i\mathrm{D}_n^{(B)}}, \tag{7b}$$

$$C_n = \frac{a^{n+1}\left[\mathrm{C}_n^{(C\sigma)}\sigma_n + \mathrm{C}_n^{(C\tau)}\tau_n\right]}{2\mu_i\mathrm{D}_n^{(C)}}, \tag{7c}$$

$$D_n = -\frac{a^{n+3}\left[\mathrm{C}_n^{(D\sigma)}\sigma_n + \mathrm{C}_n^{(D\tau)}\tau_n\right]}{2\mu_i\mathrm{D}_n^{(D)}}. \tag{7d}$$

The expressions for the coefficients $\mathrm{C}_n^{(A\sigma)}$, $\mathrm{C}_n^{(A\tau)}$, $\mathrm{D}_n^{(A)}$, $\mathrm{C}_n^{(B\sigma)}$, $\mathrm{C}_n^{(B\tau)}$, $\mathrm{D}_n^{(B)}$, $\mathrm{C}_n^{(C\sigma)}$, $\mathrm{C}_n^{(C\tau)}$, $\mathrm{D}_n^{(C)}$, $\mathrm{C}_n^{(D\sigma)}$, $\mathrm{C}_n^{(D\tau)}$, and $\mathrm{D}_n^{(D)}$ are reported in equation set (A6) of (Tagliavia et al., 2010b). Note that each coefficient depends on the inclusion material properties and geometry.

If $n = 1$, B_n vanishes, see Eqs. (A2c) and (A2d). Thus, equation set (6) becomes a linear system of four equations in three unknowns A_1, C_1, and D_1. The system can be solved by accounting for Eq. (5) to give

$$A_1 = \frac{\sigma_1}{8\mu_i a(\eta^5-1)(\nu_i+1)}, \tag{8a}$$

$$C_1 = 0, \tag{8b}$$

$$D_1 = \frac{a^4\eta^5\sigma_1}{12\mu_i(\eta^5-1)}. \tag{8c}$$

In addition, substituting equation sets (7) and (8) in Eqs. (A2a) and (A2b) gives

$$\frac{2\mu_m}{a\sigma_\infty}u_r^{(\mathrm{III})}(a,\theta) = -\beta\left\{\frac{[2(\nu_i+1)\eta^5 - 12\nu_i + 3]\sigma_1}{6(\eta^5-1)(\nu_i+1)} - \frac{2B_1\mu_i}{a}\right\}P_1(\cos\theta) - \beta\sum_{n=0,n\neq1}^{\infty}\frac{\mathrm{E}_n^{(r\sigma)}\sigma_n + \mathrm{E}_n^{(r\tau)}\tau_n}{\mathrm{F}_n^{(r)}}P_n(\cos\theta), \tag{9a}$$

$$\frac{2\mu_m}{a\sigma_\infty}u_\theta^{(\mathrm{III})}(a,\theta) = +\beta\left\{\frac{[(\nu_i+1)\eta^5 - 6\nu_i + 9]\sigma_1}{6(\eta^5-1)(\nu_i+1)} + \frac{2B_1\mu_i}{a}\right\}\frac{\mathrm{d}P_1(\cos\theta)}{\mathrm{d}\theta} - \beta\sum_{n=2}^{\infty}\frac{\mathrm{E}_n^{(\theta\sigma)}\sigma_n + \mathrm{E}_n^{(\theta\tau)}\tau_n}{\mathrm{F}_n^{(\theta)}}\frac{\mathrm{d}P_n(\cos\theta)}{\mathrm{d}\theta}, \tag{9b}$$

where $\beta = \mu_m/\mu_i$ and the expressions for the coefficients $\mathrm{E}_n^{(r\sigma)}$, $\mathrm{E}_n^{(r\tau)}$, $\mathrm{E}_n^{(\theta\sigma)}$, $\mathrm{E}_n^{(\theta\tau)}$, $\mathrm{F}_n^{(r)}$, and $\mathrm{F}_n^{(\theta)}$ are reported in equation set (A7) of (Tagliavia et al., 2010b). In equation set (9), B_1 is undetermined and it is physically related to the rigid body motion as evidenced in Eqs. (A2a) and (A2b).

4. Semi-analytical solution

4.1. Governing integral equations

By substituting equation sets (A5), (A6) and (9) in equation set (3) and using equation set (2), the following set of homogeneous Fredholm integral equations of the first kind is obtained

$$\int_{\alpha_1}^{\alpha_2}\mathcal{F}^{(r\sigma)}(\theta,\hat\theta)\tilde\sigma(\hat\theta)\mathrm{d}\hat\theta + \int_{\alpha_1}^{\alpha_2}\mathcal{F}^{(r\tau)}(\theta,\hat\theta)\tilde\tau(\hat\theta)\mathrm{d}\hat\theta = \chi_r(\theta,B_1), \tag{10a}$$

$$\int_{\alpha_1}^{\alpha_2}\mathcal{F}^{(\theta\sigma)}(\theta,\hat\theta)\tilde\sigma(\hat\theta)\mathrm{d}\hat\theta + \int_{\alpha_1}^{\alpha_2}\mathcal{F}^{(\theta\tau)}(\theta,\hat\theta)\tilde\tau(\hat\theta)\mathrm{d}\hat\theta = \chi_\theta(\theta,B_1), \tag{10b}$$

Here, $\tilde\sigma(\theta) = \sigma(\theta)/\sigma_\infty$ and $\tilde\tau(\theta) = \tau(\theta)/\sigma_\infty$ are the relative radial and shear stress fields at the interface, $\chi_r(\theta,B_1)$ and $\chi_\theta(\theta,B_1)$ are defined in Eqs. (A9b) and (A9c), respectively, and $\mathcal{F}^{(r\sigma)}(\theta,\hat\theta)$, $\mathcal{F}^{(r\tau)}(\theta,\hat\theta)$, $\mathcal{F}^{(\theta\sigma)}(\theta,\hat\theta)$, and $\mathcal{F}^{(\theta\tau)}(\theta,\hat\theta)$ are the Fredholm kernels given by

$$\mathcal{F}^{(r\sigma)}(\theta,\hat{\theta}) = \sin\hat{\theta}\sum_{n=0,n\neq1}^{\infty}\frac{(2n+1)}{2}\left(\frac{\mathsf{A}_n^{(r\sigma)}}{\mathsf{B}_n^{(r)}}+\beta\frac{\mathsf{E}_n^{(r\sigma)}}{\mathsf{F}_n^{(r)}}\right)P_n(\cos\theta)P_n(\cos\hat{\theta}) + \frac{1}{4}\left\{\frac{\beta[2(v_i+1)\eta^5-12v_i+3]}{(\eta^5-1)(v_i+1)}-\frac{2(8v_m-7)}{3(v_m-1)}\right\} \times \sin\hat{\theta}P_1(\cos\theta)P_1(\cos\hat{\theta}), \tag{11a}$$

$$\mathcal{F}^{(r\tau)}(\theta,\hat{\theta}) = \sin\hat{\theta}\sum_{n=2}^{\infty}\frac{2n+1}{2n(n+1)}\left(\frac{\mathsf{A}_n^{(r\tau)}}{\mathsf{B}_n^{(r)}}+\beta\frac{\mathsf{E}_n^{(r\tau)}}{\mathsf{F}_n^{(r)}}\right)P_n(\cos\theta)\frac{\mathrm{d}P_n(\cos\hat{\theta})}{\mathrm{d}\theta} + \frac{4-5v_m}{6(v_m-1)}\sin\hat{\theta}P_1(\cos\theta)\frac{\mathrm{d}P_1(\cos\hat{\theta})}{\mathrm{d}\hat{\theta}}, \tag{11b}$$

$$\mathcal{F}^{(\theta\sigma)}(\theta,\hat{\theta}) = \sin\hat{\theta}\sum_{n=0,n\neq1}^{\infty}\frac{(2n+1)}{2}\left(\frac{\mathsf{A}_n^{(\theta\sigma)}}{\mathsf{B}_n^{(\theta)}}+\beta\frac{\mathsf{E}_n^{(\theta\sigma)}}{\mathsf{F}_n^{(\theta)}}\right)\frac{\mathrm{d}P_n(\cos\theta)}{\mathrm{d}\theta} \times P_n(\cos\hat{\theta})+\frac{3}{2}\left\{\frac{4-5v_m}{9(v_m-1)}-\frac{\beta[(v_i+1)\eta^5-6v_i+9]}{6(\eta^5-1)(v_i+1)}\right\} \times \sin\hat{\theta}\frac{\mathrm{d}P_1(\cos\theta)}{\mathrm{d}\theta}P_1(\cos\hat{\theta}), \tag{11c}$$

$$\mathcal{F}^{(\theta\tau)}(\theta,\hat{\theta}) = \sin\hat{\theta}\sum_{n=2}^{\infty}\frac{2n+1}{2n(n+1)}\left(\frac{\mathsf{A}_n^{(\theta\tau)}}{\mathsf{B}_n^{(\theta)}}+\beta\frac{\mathsf{E}_n^{(\theta\tau)}}{\mathsf{F}_n^{(\theta)}}\right)\frac{\mathrm{d}P_n(\cos\theta)}{\mathrm{d}\theta} \times\frac{\mathrm{d}P_n(\cos\hat{\theta})}{\mathrm{d}\hat{\theta}}+\frac{11-13v_m}{12(v_m-1)}\sin\hat{\theta}\frac{\mathrm{d}P_1(\cos\theta)}{\mathrm{d}\theta}\frac{\mathrm{d}P_1(\cos\hat{\theta})}{\mathrm{d}\hat{\theta}}. \tag{11d}$$

4.2. Enriched Galerkin method

A numerical solution of the integral equation set (10) is computed by using an approach based on the Galerkin method (see for example Babolian and Delves, 1979). In particular, the interfacial stress fields are expanded in terms of linear combinations of independent basis functions in the solution space. The coefficients in the expansion are determined by projecting Eqs. (10a) and (10b) onto the basis sets. More specifically, the stress fields are expressed as

$$\tilde{\sigma}(\theta) = \sum_{n=0}^{d+1}\omega_n^{(\sigma)}\rho_n^{(\sigma)}(\theta), \tag{12a}$$

$$\tilde{\tau}(\theta) = \sum_{n=0}^{d+1}\omega_n^{(\tau)}\rho_n^{(\tau)}(\theta), \tag{12b}$$

where $\left\{\omega_n^{(\sigma)}\right\}_{n=0}^{d+1}$ and $\left\{\omega_n^{(\tau)}\right\}_{n=0}^{d+1}$ are unknown coefficients, $\left\{\rho_n^{(\sigma)}(\theta)\right\}_{n=0}^{d+1}$ and $\left\{\rho_n^{(\tau)}(\theta)\right\}_{n=0}^{d+1}$ denote the basis functions, and $2d+4$ is the total number of basis functions used for the approximation. The coefficients $\left\{\omega_n^{(\sigma)}\right\}_{n=0}^{d+1}$ and $\left\{\omega_n^{(\tau)}\right\}_{n=0}^{d+1}$ are determined by solving the following set of $2d+4$ linear equations

$$\sum_{n=0}^{d+1}\omega_n^{(\sigma)}\int_{\alpha_1}^{\alpha_2}\int_{\alpha_1}^{\alpha_2}\mathcal{F}^{(r\sigma)}(\theta,\hat{\theta})\rho_n^{(\sigma)}(\hat{\theta})\rho_r^{(\sigma)}(\theta)\mathrm{d}\theta\mathrm{d}\hat{\theta} + \sum_{n=0}^{d+1}\omega_n^{(\tau)}\int_{\alpha_1}^{\alpha_2}\int_{\alpha_1}^{\alpha_2}\mathcal{F}^{(r\tau)}(\theta,\hat{\theta})\rho_n^{(\tau)}(\hat{\theta})\rho_r^{(\sigma)}(\theta)\mathrm{d}\theta\mathrm{d}\hat{\theta} = -\int_{\alpha_1}^{\alpha_2}\frac{2\mu_m}{a\sigma_\infty}u_r^{(\mathrm{I})}(a,\theta)\rho_r^{(\sigma)}(\theta)\mathrm{d}\theta + \frac{2\beta B_1\mu_i}{a}\int_{\alpha_1}^{\alpha_2}\cos\theta\rho_r^{(\sigma)}(\theta)\mathrm{d}\theta, \tag{13a}$$

$$\sum_{n=0}^{d+1}\omega_n^{(\sigma)}\int_{\alpha_1}^{\alpha_2}\int_{\alpha_1}^{\alpha_2}\mathcal{F}^{(\theta\sigma)}(\theta,\hat{\theta})\rho_n^{(\sigma)}(\hat{\theta})\rho_r^{(\tau)}(\theta)\mathrm{d}\theta\mathrm{d}\hat{\theta} + \sum_{n=0}^{d+1}\omega_n^{(\tau)}\int_{\alpha_1}^{\alpha_2}\int_{\alpha_1}^{\alpha_2}\mathcal{F}^{(\theta\tau)}(\theta,\hat{\theta})\rho_n^{(\tau)}(\hat{\theta})\rho_r^{(\tau)}(\theta)\mathrm{d}\theta\mathrm{d}\hat{\theta} = -\int_{\alpha_1}^{\alpha_2}\frac{2\mu_m}{a\sigma_\infty}u_\theta^{(\mathrm{I})}(a,\theta)\rho_r^{(\tau)}(\theta)\mathrm{d}\theta - \frac{2\beta B_1\mu_i}{a}\int_{\alpha_1}^{\alpha_2}\sin\theta\rho_r^{(\tau)}(\theta)\mathrm{d}\theta. \tag{13b}$$

For convenience, equation set (13) can be rewritten in the matrix form as follows

$$\mathbf{F}\boldsymbol{\omega} = \boldsymbol{\chi}(B_1), \tag{14}$$

where the expressions of the matrix $\mathbf{F}$ and the column vectors $\boldsymbol{\omega}$ and $\boldsymbol{\chi}(B_1)$ are reported in Eq. (A7) and equation set (A9). Recalling equation sets (2) and (12), Eq. (5) becomes

$$\boldsymbol{\kappa}^{\mathrm{T}}\boldsymbol{\omega} = 0, \tag{15}$$

where $\boldsymbol{\kappa}$ is given by Eq. (A9e). Finally, manipulating Eq. (14) and substituting Eq. (15), B_1 is obtained through

$$\boldsymbol{\kappa}^{\mathrm{T}}\mathbf{F}^{-1}\boldsymbol{\chi}(B_1) = 0. \tag{16}$$

Once B_1 is determined, a solution for the linear system in equation set (13) is found.

Dealing with interfacial cracks requires coping with singularities and oscillations of the stress fields in proximity of the cracks' tips (Kuang and Wang, 1999). Thus, the basis sets are enriched by special functions that allow for describing these behaviors (see for example Ching and Batra, 2001; Fleming et al., 1997). As suggested in Martynenko and Lebedyeva (2006), radial and circumferential stress fields in the crack tip proximity can be expressed as a linear combination of two suitable functions, (see for example Tagliavia et al., 2010b). In this study, two different cracks defined by the crack tip angles α_1 and α_2 are considered. Therefore, four pairs of special functions are used to enrich the basis sets, namely,

$$\rho_0^{(\sigma)}(\theta) = \rho_0^{(\tau)}(\theta) = \frac{\sin\left[\gamma\log\left(\sin\frac{\theta}{2}-\sin\frac{\alpha_1}{2}\right)\right]}{\sqrt{\sin\frac{\theta}{2}-\sin\frac{\alpha_1}{2}}}, \tag{17a}$$

$$\rho_1^{(\sigma)}(\theta) = \rho_1^{(\tau)}(\theta) = \frac{\cos\left[\gamma\log\left(\sin\frac{\theta}{2}-\sin\frac{\alpha_1}{2}\right)\right]}{\sqrt{\sin\frac{\theta}{2}-\sin\frac{\alpha_1}{2}}}, \tag{17b}$$

$$\rho_2^{(\sigma)}(\theta) = \rho_2^{(\tau)}(\theta) = \frac{\sin\left[\gamma\log\left(\cos\frac{\theta}{2}-\cos\frac{\alpha_2}{2}\right)\right]}{\sqrt{\cos\frac{\theta}{2}-\cos\frac{\alpha_2}{2}}}, \tag{17c}$$

$$\rho_3^{(\sigma)}(\theta) = \rho_3^{(\tau)}(\theta) = \frac{\cos\left[\gamma\log\left(\cos\frac{\theta}{2}-\cos\frac{\alpha_2}{2}\right)\right]}{\sqrt{\cos\frac{\theta}{2}-\cos\frac{\alpha_2}{2}}}. \tag{17d}$$

Here, γ is the mismatch parameter defined in Dundurs (1969) as

$$\gamma = \frac{1}{2\pi}\log\frac{3\beta+1-4\beta v_i}{3+\beta-4v_m}. \tag{18}$$

Note that when the two materials share the same elastic properties $\beta = 1$ and γ vanishes. The remaining smooth functions $\left\{\rho_n^{(\sigma)}(\theta)\right\}_{n=4}^{d+1}$ and $\left\{\rho_n^{(\tau)}(\theta)\right\}_{n=4}^{d+1}$ are selected consistently with (Tagliavia et al., 2010b) for computational efficiency. Note that, by taking α_1 nonzero and $\alpha_2 = 180°$, the problem of two spherical-cap cracks reduces to the problem of a single crack. In this case, Eqs. (17c) and (17d) are discarded and the basis sets are consistently depleted.

5. Energetics of a system of cracks

Here, energetics and stability criteria for crack propagation are discussed. More specifically, growth and interaction of cracks are studied by analyzing ERRs and their variations. Note that the overarching analysis is limited to crack growth along the particle-matrix interface.

5.1. Energy release rate

By following the classical Griffith's linear elastic theory for brittle materials (Griffith, 1921) and by assuming a constant prescribed applied load, the ERR can be expressed as follows (see for example Gdoutos, 2005),

$$\mathrm{G} = -\frac{1}{a^2}\frac{\partial \Pi}{\partial \Gamma} = \frac{1}{a^2}\frac{\partial U}{\partial \Gamma}. \tag{19}$$

Here, Π is the potential energy, U is the elastic energy stored in the material that equals -Π, and Γ is the crack surface area normalized by a^2. For glass-vinyl ester syntactic foams, the assumptions of brittle fracture and linear elastic behavior are consistent with experimental observations under tensile and flexural loading (Gupta et al., 2010; Tagliavia et al., 2010a). Note that this quantity is occasionally referred to as the strain energy release rate, (see for example Gdoutos, 2005).

The elastic energy stored in the composite is computed by using the Eshelby's decomposition (see for example Christensen, 1979),

$$U = U^0 + U_{\mathrm{INT}}, \tag{20}$$

where U^0 is the energy stored in case the inclusion is replaced by the matrix material and U_{INT} is the energy stored in the composite due to the particle-matrix interaction through the interface. According to Eshelby's formula, U_{INT} can be computed from the stress and displacement fields at the particle-matrix interface by

$$\begin{aligned} U_{\mathrm{INT}} = {} & \pi \int_0^{\pi} \left[\sigma^0_{rr}(a,\theta)u_r(a^+,\theta) + \tau^0_{r\theta}(a,\theta)u_\theta(a^+,\theta)\right] a^2 \sin\theta \mathrm{d}\theta \\ & - \pi \int_0^{\pi} \left[\sigma(\theta)u^0_r(a,\theta) + \tau(\theta)u^0_\theta(a,\theta)\right] a^2 \sin\theta \mathrm{d}\theta. \end{aligned} \tag{21}$$

Here, the superscript 0 refers to the fields computed in case the matrix material replaces the particle, while the other fields are computed by solving the single inclusion problem outlined in Section 3. Note that $\sigma^0_{rr}(a,\theta)$, $\tau^0_{r\theta}(a,\theta)$, $u^0_r(a,\theta)$, and $u^0_\theta(a,\theta)$ can be determined in closed form. In addition, the overall effective compliance along the loading direction is obtained by manipulating Eq. (20) as reported in Tagliavia et al. (2010b), that is,

$$\mathcal{S} = \frac{3}{2}U_{\mathrm{INT}}\frac{E_m}{\pi a^3 \sigma^2_\infty}. \tag{22}$$

Here, $\mathcal{S} = (E_m/E_{\mathrm{eff}} - 1)/\Phi$ is the change in the relative effective elastic compliance per unit particle volume fraction, E_{eff} is the effective elastic modulus along the loading direction, and Φ is the particle volume fraction. The estimate in Eq. (22) is expected to be accurate only for small particle volume fraction due to the dilute nature of the problem under investigation. Note that $\mathcal{S}$ depends on Φ through U^0, see Tagliavia et al. (2010b), while it is a function of Γ_1 and Γ_2 through U_{INT}.

By recalling Eq. (20) and by using $\partial U^0/\partial\Gamma = 0$, Eq. (19) yields

$$\mathcal{G} = \frac{E_m}{a\sigma^2_\infty}\mathrm{G} = \frac{E_m}{a^3\sigma^2_\infty}\frac{\partial U_{\mathrm{INT}}}{\partial \Gamma}, \tag{23}$$

where $\mathcal{G}$ is a dimensionless ERR. In a system of two interacting cracks, the elastic energy stored in the material can be expressed as a function of the normalized surface areas $\Gamma_1 = 2\pi(1-\cos\alpha_1)$ and $\Gamma_2 = 2\pi(1+\cos\alpha_2)$ corresponding to the crack tip angles α_1 and α_2, respectively. Therefore, the ERR associated with each crack is defined as (Nemat-Nasser, 1978)

$$\mathcal{G}_i = \frac{E_m}{a\sigma^2_\infty}\mathrm{G}_i = \frac{E_m}{a^3\sigma^2_\infty}\frac{\partial U_{\mathrm{INT}}}{\partial \Gamma_i}, \quad i = 1,2. \tag{24}$$

5.2. Crack growth

According to the Griffith fracture condition, propagation of the ith crack, with $i = 1, 2$, is initiated if the total potential energy is stationary with respect of the ith crack surface area, that is,

$$\frac{1}{a^2}\frac{\partial(\Pi + \Delta_i)}{\partial \Gamma_i} = -\mathrm{G}_i + \mathcal{R}_i = 0. \tag{25}$$

Here, Δ_i is the energy dissipated in the crack propagation and $\mathcal{R}_i = \partial\Delta_i/\partial\Gamma_i$ is the energy required to form one unit of new surface area. $\mathcal{R}_1 = \mathcal{R}_2 = \mathcal{R}$ is assumed to be a property of the interface (see for example Guo and Sun, 1997; Hamoush and Ahmad, 1989; Marotzke and Qiao, 1997). Simultaneous crack propagation occurs if $\mathrm{G}_1 = \mathrm{G}_2 = \mathcal{R}$. Crack growth is defined to be stable if propagation is not spontaneous (Nemat-Nasser, 1978), that is, cracks propagate only if the applied load is increased.

The analysis of the sign of $\partial\mathcal{G}_i/\partial\Gamma_i$ is sufficient to assess the stability of the growth of the ith crack as the other crack is held fixed. More specifically, if $\partial\mathcal{G}_i/\partial\Gamma_i$ is positive the growth is unstable and is stable if $\partial\mathcal{G}_i/\partial\Gamma_i$ is negative. On the other hand, the stability of the system of two crack is studied by means of the second variation of Π for any admissible perturbation of crack surface areas $\delta\Gamma_1$ and $\delta\Gamma_2$ (Suo and Combescure, 1992; Suo and Valeta, 1998), that is,

$$\begin{aligned} & \sum_{i,j=1}^{2}\frac{\partial^2\Pi}{\partial\Gamma_i\partial\Gamma_j}\delta\Gamma_i\delta\Gamma_j \\ & = -\sum_{i,j=1}^{2}\frac{\partial^2 U}{\partial\Gamma_i\partial\Gamma_j}\delta\Gamma_i\delta\Gamma_j \begin{cases} >0, & \text{stable} \\ =0, & \text{critical} \quad \forall\ \delta\Gamma_1 \geqslant 0 \ \text{and} \ \delta\Gamma_2 \geqslant 0. \\ <0, & \text{unstable} \end{cases} \end{aligned} \tag{26}$$

Since U_{INT} is a symmetric function of Γ_1 and Γ_2, crack configurations with $\Gamma_1 = \Gamma_2$ satisfy $\mathrm{G}_1 = \mathrm{G}_2$, see Eq. (24). These crack configurations are analyzed in what follows and identified by $\Gamma_e = \Gamma_1 = \Gamma_2$. By using the symmetry of U_{INT} with respect to Γ_1 and Γ_2, the stability of Γ_e is expressed in terms of the dimensionless ERRs through

$$\begin{cases} \partial\mathcal{G}_1/\partial\Gamma_1 = \partial\mathcal{G}_2/\partial\Gamma_2 > 0, & \text{unstable}, \\ \partial\mathcal{G}_1/\partial\Gamma_1 < 0 \quad \text{and} \quad \partial\mathcal{G}_1/\partial\Gamma_2 = \partial\mathcal{G}_2/\partial\Gamma_1 < 0, & \text{stable}, \\ \partial\mathcal{G}_1/\partial\Gamma_1 < 0 \quad \text{and} \quad 0 < \partial\mathcal{G}_1/\partial\Gamma_2 < |\partial\mathcal{G}_1/\partial\Gamma_1|, & \text{stable}. \end{cases} \tag{27}$$

Stability of a similar system of cracks is studied in Bazant and Tabbara (1992) and Sumi et al. (1980).

Interfacial crack growth characteristics are determined by minimizing the potential energy Π. This is achieved by adapting the constrained quadratic programming on virtual crack extension presented in Hwang and Ingraffea (2004). For the two crack problem, the quadratic programming optimization with a linear equality constraint and bounds reads

$$\begin{aligned} & \text{Maximize} \quad \sum_{i=1}^{2}\mathcal{G}_i\delta\Gamma_i \ \text{with respect to} \ \delta\Gamma_1 \ \text{and} \ \delta\Gamma_2, \\ & \text{subjected to} \quad \sum_{i=1}^{2}\delta\Gamma_i = c \ \forall\delta\Gamma_1 \geqslant 0 \ \text{and} \ \delta\Gamma_2 \geqslant 0, \end{aligned} \tag{28}$$

where c is a constant defining the overall surface area generation. Note that crack surface perturbations in Eq. (28) refer only to propagation and not closing.

6. Results and discussion

Here, the semi-analytical solution presented in Section 4 is used to compute stress and displacement fields at the particle-matrix interface. These fields are used to evaluate the interaction energy defined by Eq. (21). Numerical simulations are performed by using a FORTRAN90 code for a variety of crack configurations and particle wall thicknesses. Crack tip angles α_1 and α_2 are varied in steps of 5° in the ranges [5°,60°] and [120°,180°], respectively, and further in steps of 1° in the ranges [60°,70°] and [110°,120°] to better assess the interaction of the cracks as the crack tips approach each other. Numerical results for equal crack configurations, that is, scenarios in which $\alpha_1 = \pi - \alpha_2$, are taken from (Tagliavia et al., 2010b). The number of independent configurations is reduced to half by noticing that crack configurations identified by the angle pairs (α_1, α_2) and $(\pi - \alpha_2, \pi - \alpha_1)$ are equivalent. For the selected ranges of α_1 and α_2, both Γ_1 and Γ_2 vary in the interval [0,4.13].

Kernels of the integrals in equation set (13) are numerically approximated. Numerical analyses show that the matrix **F** is non-singular and the solutions for the stress and displacements fields are accurate if d is set to 7 and 400 or more terms are retained in the kernels. Note that for $\alpha_2 = 180°$, d reduces to 5. The ERR is computed by fitting U_{INT} with a 8th order polynomial of even powers of the crack surface area and differentiating by following Eq. (24).

The role of particle wall thickness is investigated for a wide range of η that spans between quasi-solid ($\eta = 0.1$) to very thin-walled inclusions ($\eta = 0.94$). The matrix **F** can be written as the linear combination of matrices whose entries are independent of η, see for example Eq. (A7) and equation set (A8). Determining such entries requires numerical integration that, nevertheless, depends only on the crack configuration. Thus, parametric studies on the effect of wall thickness are easily implemented in the enriched Galerkin method providing an advantage with respect to FEA, where changing the problem geometry requires addressing a different representative volume element.

Glass-vinyl ester syntactic foam system is selected as reference in the further discussion. Accordingly, numerical results are computed using $E_m = 3.21$ GPa, $\nu_m = 0.3$, $E_i = 60$ GPa, and $\nu_i = 0.21$ as reported in Tagliavia et al. (2010a). The corresponding material mismatch parameters are $\beta = 4.98 \times 10^{-2}$ and $\gamma = -8.16 \times 10^{-2}$. In addition, particle of one unit outer radius is selected in the geometry.

6.1. Stable growth of equal cracks

Based on Eq. (27), the stability of the simultaneous propagation of two equal cracks is analyzed. Numerical analysis shows that the system is unstable for low values of Γ_e and stable after crossing a threshold $\Gamma_e = \Gamma_{st}$ for any particle wall thickness. The position of the threshold value depends on η. More specifically, Γ_{st} increases from 2.27 to 3.55 as η increases from 0.1 to 0.94, thus causing a reduction in the stable crack growth region. Note that the corresponding values (α_1, α_2) for $\Gamma_{st} = 2.27$ and $\Gamma_{st} = 3.55$ are (50.26°,129.74°) and (64.27°,115.73°), respectively. Numerical findings on solid particle filled composites reported in Benabou et al. (2005) and Cho et al. (2006) are in line with the semi-analytical results for $\eta = 0.1$ presented here.

The behavior of a representative unstable crack configuration $\Gamma_e = 0.28$ corresponding to $\alpha_1 = 17°$ is described by means of the ERRs in Fig. 2. For $\eta = 0.1$, Fig. 2 shows $\mathcal{G}_i$ and $\mathcal{G}_j$ as functions of Γ_i for $\Gamma_j = 0.28$ and $i, j = 1, 2$ with $i \neq j$. The intersection of $\mathcal{G}_i$ and $\mathcal{G}_j$ corresponds to the crack configuration $\Gamma_e = 0.28$. As shown in Fig. 2, a small positive Γ_2 perturbation from the equilibrium produces an increment of $\mathcal{G}_2$ and a decrease in $\mathcal{G}_1$, and viceversa. Thus,

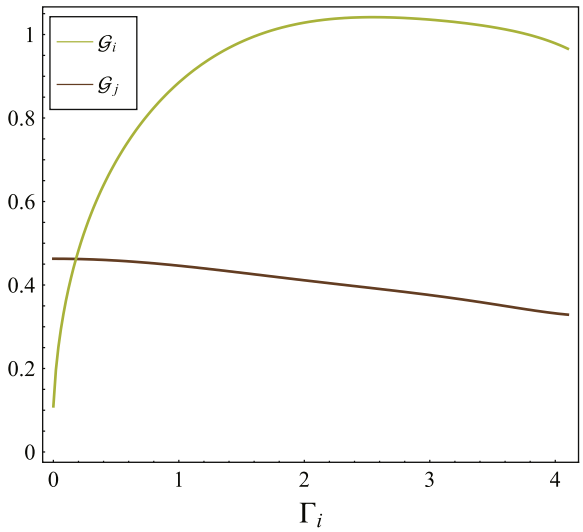

Fig. 2. $\mathcal{G}_i$ and $\mathcal{G}_j$ as functions of Γ_i for $\eta = 0.1$, $\Gamma_j = 0.28$, and $i, j = 1, 2$ with $i \neq j$.

only the perturbed crack is able to propagate. In addition, Fig. 2 shows that $\mathcal{G}_1 = \mathcal{G}_2$ only if $\Gamma_1 = \Gamma_2$. Similar behavior is found for any selection of η, showing that simultaneous crack propagation is only possible if $\Gamma_1 = \Gamma_2$.

6.2. Crack growth characteristics

By applying the algorithm in Eq. (28) to the two crack problem and selecting $c = 0.02$ corresponding to 0.16% of the particle outer surface area, characteristics of crack growth for the case of a quasi-solid inclusion ($\eta = 0.1$) are obtained and presented in Fig. 3 as functions of Γ_1 and Γ_2.

The graph shows the presence of two regions, labeled as $\mathbb{A}$ and $\mathbb{B}$, corresponding to crack configurations that evolve by increasing Γ_2 and Γ_1, respectively. The inversion of the regions $\mathbb{A}$ and $\mathbb{B}$ with respect to the set of equal crack configurations, named $\mathbb{D}$, for $\Gamma_e > 3.66$ identifies the transition from individual to equal crack growth. For $i = 1$, 2, any positive perturbation on Γ_i of a crack

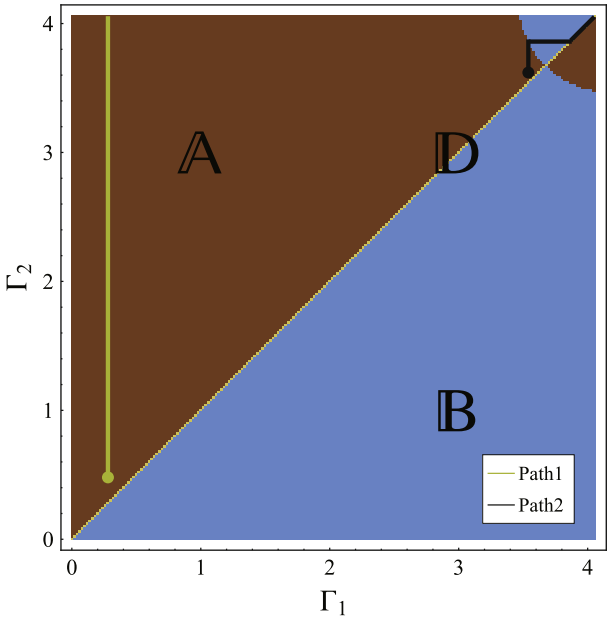

Fig. 3. Numerically predicted crack growth evolutions for $\eta = 0.1$.

configuration with $\Gamma_e < 3.66$ provides an increment in Γ_i. Thus, the perturbation causes a symmetry breaking. Conversely, any positive Γ_2 perturbation of a crack configuration with $\Gamma_e > 3.66$ provides an increment in Γ_1 and viceversa. Thus, the system propagates by reestablishing the symmetric configuration $\Gamma_1 = \Gamma_2$. Numerical results are largely independent of c within the investigated range of $[0.01, 0.06]$.

The analysis in Fig. 3 can be complemented with tensile stress–strain plots that describe the composite overall response to crack propagation. As an example, two widely different initial crack configurations of $(17°, 158°)$ and $(64°, 115°)$ and the corresponding crack growth paths, named Path1 and Path2, are considered to describe stable and unstable crack growths, see Fig. 3. Crack propagation starts when the ERR of the leading crack is equal to $\mathcal{R}$, see Eq. (25). Thus, the remote stress increases linearly with the strain until crack propagation initiates. The slope of the stress–strain graph is given by the composite effective elastic modulus E_{eff} that depends on Φ, see Eq. (22). Fig. 4a depicts stress–strain graphs for $\Phi = 0.1$ and $\mathcal{R} = 1.3$ MPa mm. The value of $\mathcal{R}$ is selected to be in line with fracture toughness and tensile strength data on glass-polymer syntactic foams (see for example Gupta et al., 2010; Wouterson et al., 2005). Note that the initial slopes are different since E_{eff} depends on Γ_1 and Γ_2. Once propagation is initiated, changes in the crack configurations are computed by using a control scheme on the crack surface area which allows for covering simulated crack growth branches (see for example Barpi and Valente, 1998; Saleh and Aliabadi, 1995). According to this iterative procedure, a virtual crack increment is considered and stress–strain values are computed at each step from the change in the effective elastic modulus (Carpinteri and Monetto, 1999). In other words, after the crack propagation initiates, production of crack surface area is used to compute the critical stress and the effective modulus, which are in turn used to determine the strain.

The post-critical behaviors of Path1 and Path2 are drastically different as shown in Fig. 4b and c. In particular, Path1 presents a snap-back instability, see (Bazant and Planas, 1998), due to the unstable growth that propagates in the region $\mathbb{A}$ where only Γ_2 increases. As a consequence, both stress and strain values decrease. The spontaneous crack propagation terminates at point P in Fig. 4b that corresponds to the crack configuration of $(17°, 111.5°)$. At this point, the crack ERR is equal to $\mathcal{R}$ but its rate of increase with respect to the crack extent is negative (Lee et al., 1996). After point P, the propagation is not spontaneous as shown by the increase in the stress. Similar instabilities are reported for multiple delaminations in laminated composites (see for example Andrews et al., 2006; Andrews and Massabò, 2007; Andrews and Massabò, 2008).

The post-critical behavior of Path2 is characterized by softening, see Fig. 4c. Since the initial configuration of Path2 is located in a stable zone of the region $\mathbb{A}$, crack propagation is not spontaneous. Thus, the increase of Γ_2 is possible only by increasing the stress. The change in the slope of the stress–strain graphs is due to the crack propagation. It is worth noticing that such apparently abrupt change in the curve slope does not imply a sharp modification in the composite effective modulus. Indeed, the composite effective modulus corresponds to the ratio between stress and strain rather than to the slope of the curve as per the adopted computational procedure. The approximately piecewise linear behavior of the stress–strain graph reflects a smooth decay of the stress and strain ratio from the initial slope. When $\mathcal{G}_1$ becomes larger than $\mathcal{G}_2$, the system keeps evolving in the region $\mathbb{B}$ by increasing Γ_1. Finally, after the corresponding crack configuration $\Gamma_1 = \Gamma_2$ is achieved, the cracks propagate according to an equal crack growth regime. Note that eventually the cracks are expected to kink in the matrix as the interaction between the crack tips becomes more pronounced.

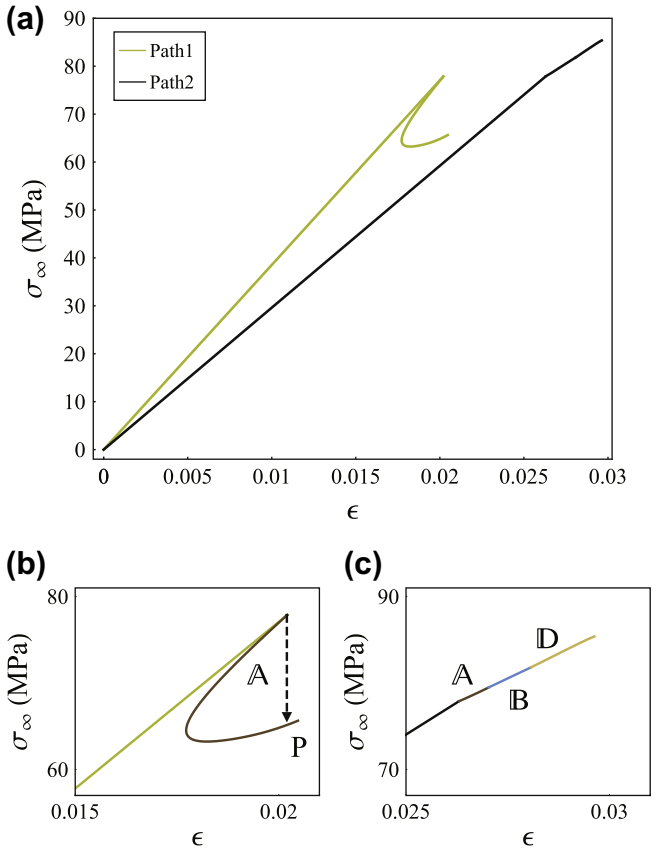

Fig. 4. (a) Stress–strain curves for crack propagation along Path1 and Path2 and close up of the post-critical behavior for (b) Path1 and (c) Path2.

6.3. Effect of crack interaction on ERRs

Comparisons of the ERR between the single and the double crack scenarios are drawn to describe the interaction between two interfacial spherical-cap cracks. The propagation of a crack in presence of another fixed crack is simulated by holding the value of α_2 constant and calculating U_{INT} for different values of α_1.

In a system of two cracks, a fixed crack modifies the propagation of the other crack leading to an amplification or a shielding effect, that is, an increase or decrease in ERR as compared to the case of a single crack. In practical terms, an amplified interfacial crack has more energy available to propagate than a single crack, thus weakening the interface. On the other hand, a shielded interfacial crack needs a higher load to initiate crack propagation, thus toughening the interface. The single crack (solid lines) and the double crack (dashed lines) cases are reported in Fig. 5 for two representative particle wall thicknesses. The tip angles of the fixed crack are selected to be $\alpha_2 = 175°$ and $\alpha_2 = 120°$ in Fig. 5a and b to describe a small and a relatively large defect, respectively. As shown in Fig. 5a, the presence of a small crack does not produce notable changes in the ERR of a single crack except for Γ_1 above 3.9. In contrast, a prominent shielding effect is observed for a relatively large crack in Fig. 5b. In this study, evidence of amplification phenomena is not found for any investigated configuration, consistently with plane strain/stress problems for arc cracks along the interface between a circular inclusion and a dissimilar infinite medium (see for example Prasad and Simha, 2002). In addition, similar findings are reported for multiple delaminations in laminated plates where amplification or shielding effects occur depending on crack extents and locations (see for example Andrews et al., 2006).

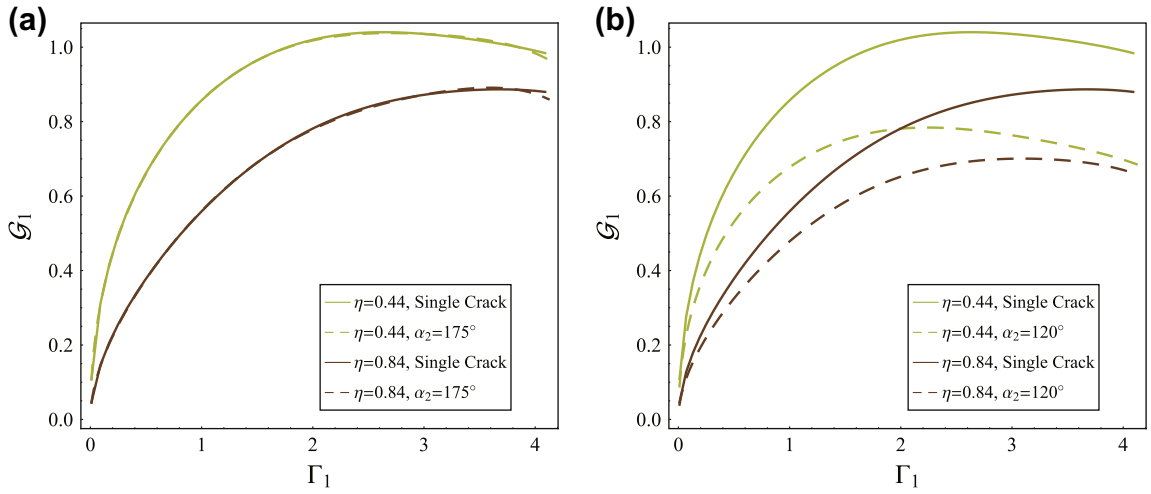

Fig. 5. Comparison of $\mathcal{G}_1$ as a function of Γ_1 between a single crack ($\alpha_2 = 180°$) and a double crack scenario with a fixed (a) $\alpha_2 = 175°$ and (b) $\alpha_2 = 120°$.

Fig. 6 shows $\mathcal{G}_1^{180}$ as a function of Γ_1 and η in a 2D contour plot. Here, the superscript 180 refers to the corresponding α_2 value, in degrees, selected in this case. The dashed line identifies the locus of the maxima of $\mathcal{G}_1^{180}$, named Γ_c, as a function of η. The existence of a maximum implies that unstable propagation transitions to stable growth after crossing the dashed line in Fig. 6 for any particle wall thickness. This behavior may be attributed to the Poisson's ratio effect, that minimizes the contribution of the opening mode on the variation of $\mathcal{G}_1^{180}$ as Γ_1 increases (Benabou et al., 2005). As the particle wall thickness decreases, Γ_c increases and the corresponding $\mathcal{G}_1^{180}$ value decreases, see Fig. 6. This implies toughening of the interface and increase of the range for stable growth. Such observations can be attributed to the fact that thinner particles act as softer reinforcements similar to those studied in Kinloch et al. (2005).

The effect of particle wall thickness on cracks' interaction is analyzed by considering the ERR of a crack propagating in presence of another fixed crack with a smaller extent, namely for $\Gamma_1 > \Gamma_2$. This builds on the observations that the larger crack generally propagates first, see Figs. 2 and 3. In Fig. 7a, $\mathcal{G}_1^{180} - \mathcal{G}_1$ is displayed as a function of Γ_2 and α_2. For each selected α_2 value, the two functions are evaluated at $\Gamma_1 = \Gamma_2 + 0.1$. Fig. 7a illustrates that $\mathcal{G}_1^{180} - \mathcal{G}_1$ is always positive, thus a shorter fixed crack generates a shielding effect regardless of Γ_2 and η. Moreover, the shielding effect increases as Γ_2 is increased or η is decreased. Similar findings are obtained by varying $\Gamma_1 - \Gamma_2$ in the range [0.1, 0.5].

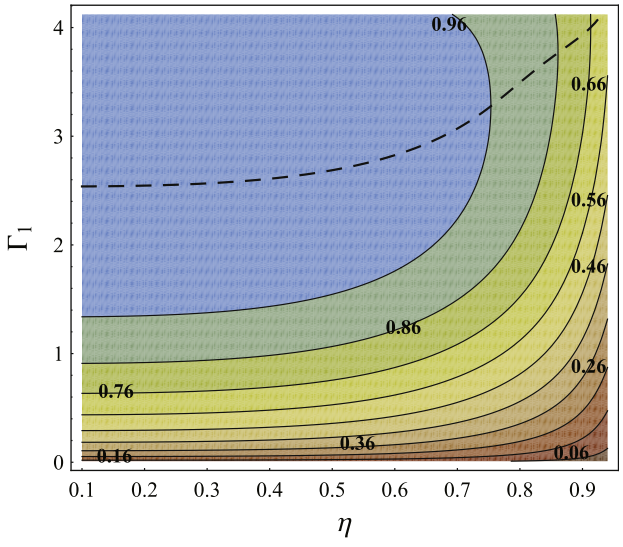

Fig. 6. $\mathcal{G}_1^{180}$ as a function of η and Γ_1 in a 2D contour plot. The dashed line identifies the locus of the maxima of $\mathcal{G}_1^{180}$.

Fig. 7b shows $\partial\mathcal{G}_1^{180}/\partial\Gamma_1$ (solid lines) and $\partial\mathcal{G}_1/\partial\Gamma_1$ (dashed lines) as functions of η for $\Gamma_1 = \Gamma_2 + 0.1$ and different α_2 values. For $\alpha_2 > 130°$, the presence of a fixed crack does not change the stability of the other crack. Both $\partial\mathcal{G}_1^{180}/\partial\Gamma_1$ and $\partial\mathcal{G}_1/\partial\Gamma_1$ are positive for the entire η range. Thus, the propagation of a crack is spontaneous irrespective of the presence of another crack on the opposite pole of the particle. On the other hand, a large fixed crack can stabilize the growth of the other crack depending on the particle wall thickness. More specifically, it is observed that $\partial\mathcal{G}_1/\partial\Gamma_1$ is negative and $\partial\mathcal{G}_1^{180}/\partial\Gamma_1$ is positive for $\eta < 0.55$ and $\alpha_2 = 130°$ and for $0.75 < \eta < 0.88$ and $\alpha_2 = 120°$, see the horizontal marker in Fig. 7b.

7. Remarks

The accuracy of the semi-analytical solution is validated with FEA results obtained using the commercial code ANSYS 11.0 and the representative volume element described in Tagliavia et al. (2010b). Results are specialized to $\eta = 0.936$, which corresponds to K46 glass particles produced by 3M, MN, that are widely used to fabricate syntactic foams (Bardella and Genna, 2001a; Gupta et al., 2010; Wouterson et al., 2005). Radial and shear stresses at the particle-matrix interface are compared in Fig. 8a and b, respectively, for four values of α_1 while α_2 is maintained constant at 175°. Generally, Fig. 8 shows a close agreement between the two solutions. The relative error for any selected field $k(\theta)$ is defined as

$$\left[\sum_{i=1}^{N}\left(k^{\mathrm{Gal}}(\theta_i) - k^{\mathrm{FEA}}(\theta_i)\right)^2\right]^{1/2}\left[\sum_{i=1}^{N}\left(k^{\mathrm{Gal}}(\theta_i)\right)^2\right]^{-1/2}, \tag{29}$$

where θ_i are the circumferential positions of the nodes used in FEA and the superscripts Gal and FEA identify the field values computed using the Galerkin and the finite element method, respectively. Errors are found to be less than 0.65% in all cases.

Fig. 9 shows comparisons of U_{INT} and $\mathcal{G}_1$ as functions of Γ_1 between three different methods, namely, the enriched Galerkin method, the finite element method, and the Galerkin method where the special functions in equation set (12) are discarded. In FEA, U_{INT} is indirectly computing by calculating $\mathcal{S}$ from the work done by the external traction and using Eq. (22); the ERR is computed using Eq. (24). Comparisons are presented for two α_2 values, 175° and 120°, in Fig. 9a and b, respectively. Omission of the

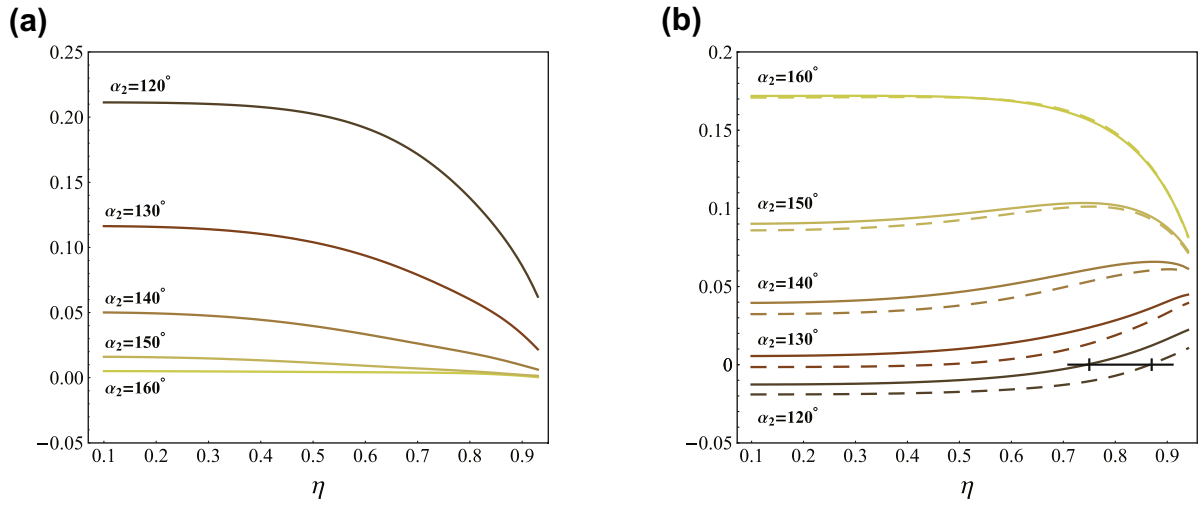

Fig. 7. (a) $\mathcal{G}_1^{180} - \mathcal{G}_1$ as a function of η for $\Gamma_1 = \Gamma_2 + 0.1$ and different α_2 values. (b) Comparisons between $\partial\mathcal{G}_1^{180}/\partial\Gamma_1$ (solid lines) and $\partial\mathcal{G}_1/\partial\Gamma_1$ (dashed lines) as functions of η for $\Gamma_1 = \Gamma_2 + 0.1$ and different α_2 values.

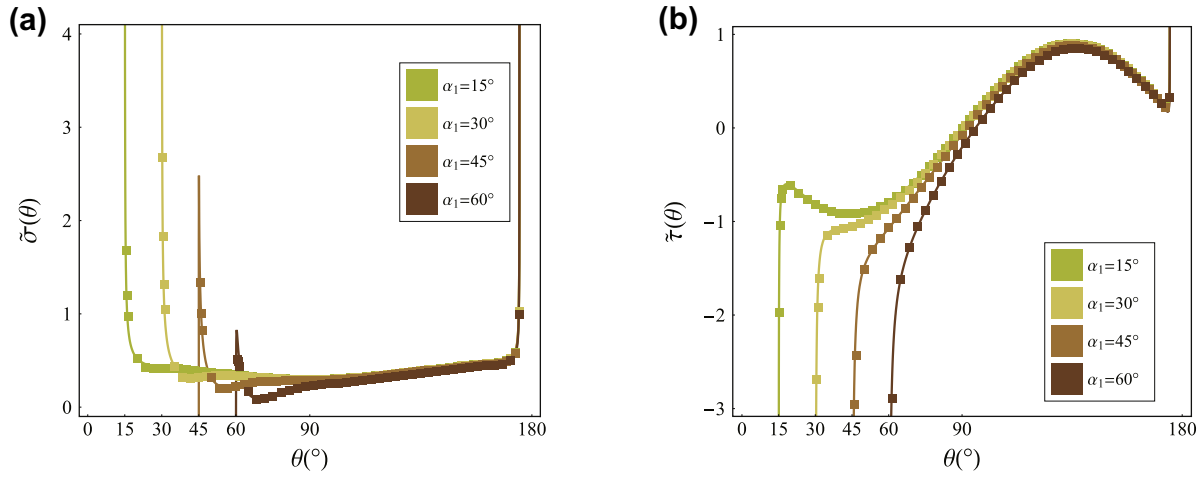

Fig. 8. Comparison of (a) normalized radial stress and (b) normalized shear stress at the particle-matrix interface as functions of θ between FEA results (squares) and Galerkin method predictions (solid lines) for $\alpha_2 = 175°$, $d = 7$, and $\eta = 0.936$. Semi-analytical solutions are plotted 0.001° away from crack tips.

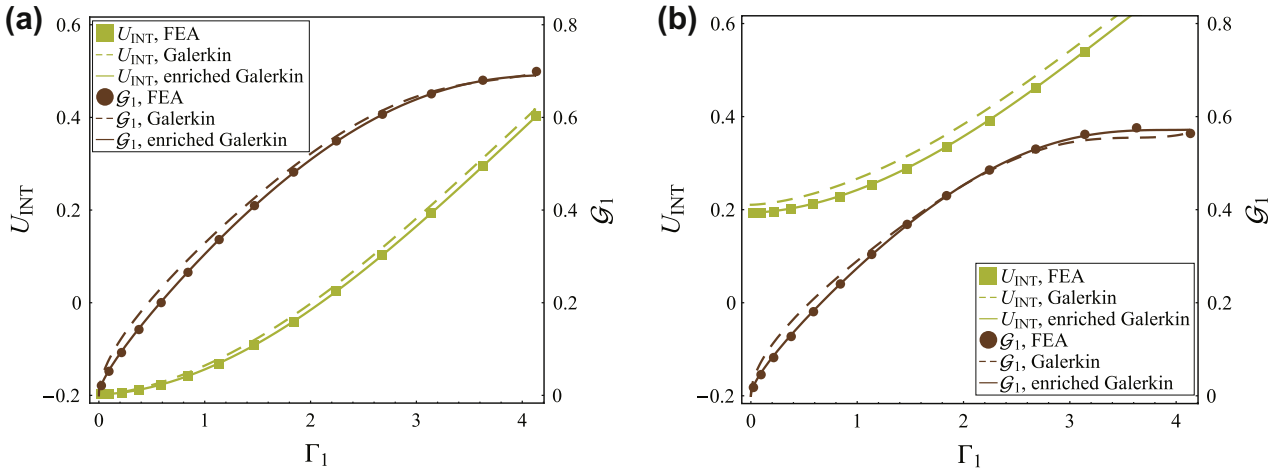

Fig. 9. U_{INT} and $\mathcal{G}_1$ computed with three different methods for $\eta = 0.936$ and (a) $\alpha_2 = 175°$ and (b) $\alpha_2 = 120°$. Solid lines identify the enriched Galerkin method, dashed lines the Galerkin method, and dots the FEA results.

singularity functions overestimates the elastic energy of interaction between the particle and the matrix for any value of α_2, see Fig. 9. The resulting difference varies in the ranges 0.11–61% and 6–11% for $\alpha_2 = 175°$ and $\alpha_2 = 120°$, respectively. The difference

between the enriched and standard Galerkin methods is noticeable for ERR results, that are based on indirect computations. Considerable discrepancies are also observed in stress distributions that show errors as large as 60% as per the definition in Eq. (29). On the other hand, for all cases under investigation, the difference between the enriched Galerkin method and FEA results is less than 2.25%.

Fig. 10 illustrates the subset of crack configurations Γ_e, named Γ_{ss}, that identifies the passage from individual to equal crack growth along with the set Γ_{st} as functions of η. As η varies from 0.1 to 0.94, Γ_{ss} increases from 3.66 to 3.86. The values of (α_1, α_2) corresponding to $\Gamma_{ss} = 3.66$ and $\Gamma_{ss} = 3.86$ are $(65.8°, 114.2°)$ and $(69°, 111°)$, respectively. In general, the quantity Γ_{st} cannot be computed by considering two equal crack as in Tagliavia et al. (2010b) due to the nature of conditions in Eq. (27) where mixed derivatives appear. Nevertheless, in this study it is found that $\partial\mathcal{G}_1/\partial\Gamma_2 = \partial\mathcal{G}_2/\partial\Gamma_1 < 0$ for any Γ_e. For $\Gamma_e < \Gamma_{st}$ the system in unstable for any particle wall thickness. For $\Gamma_{st} < \Gamma_e < \Gamma_{ss}$, the system is stable but the crack propagation features the growth of an individual crack. Finally, stability and equal crack growth are guaranteed when $\Gamma_e > \Gamma_{ss}$. Note that the difference between Γ_{ss} and Γ_{st} decreases as η increases.

The effect of the interfacial spherical-cap crack curvature on the ERR is investigated by comparison with a penny-shaped crack at the interface of two elastic half-spaces subjected to a remote tensile loading perpendicular to the interface (see for example Rice, 1988). Following (Chiu and Lin, 2009; Gosz et al., 1998), the ERR of an interfacial penny-shaped crack, named G_{ps}, is obtained as

$$G_{ps} = \frac{\pi}{4\mu_m}\frac{(1+3\beta-4\beta\nu_i)(3+\beta-4\nu_m)}{4\beta(1-\nu_i)+4(1-\nu_m)}|K|^2, \tag{30}$$

where K is the complex stress intensity factor expressed by Kassir and Bregman (1972)

$$K = 2\sigma_\infty\frac{\sqrt{t}}{\sqrt{\pi}}\frac{\Upsilon(2-\imath\gamma)}{\Upsilon(\frac{1}{2}-\imath\gamma)}, \tag{31}$$

where t is the radius of the penny-shaped crack, $\imath = \sqrt{-1}$, and Υ is the Euler's Gamma function (see for example Abramowitz and Stegun, 1965). When the elastic material properties of the two media are equal, Eq. (31) reduces to the stress intensity factor of a penny shaped crack in a homogeneous material reported in Sneddon (1979) and Eq. (30) reduces to the corresponding ERR (see for example Huang, 1995; Taya, 1981). Note that the dimensionless ERR of a penny shaped crack, named $\mathcal{G}_{ps}$, is obtained from Eq. (30) as follows

$$\mathcal{G}_{ps} = \frac{E_{eff}}{a\sigma_\infty^2}G_{ps}. \tag{32}$$

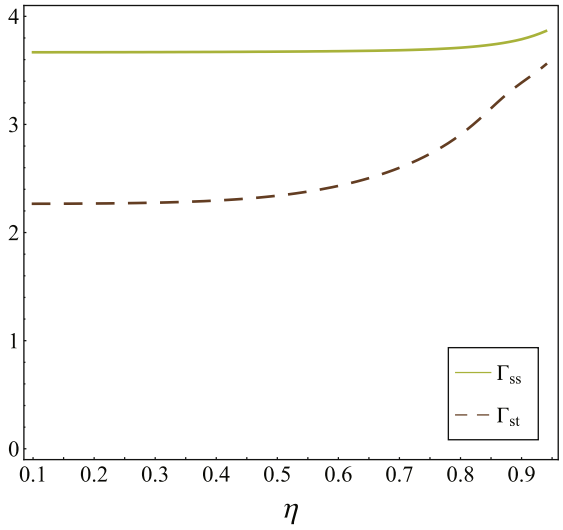

Fig. 10. Γ_{st} and Γ_{ss} as functions of η.

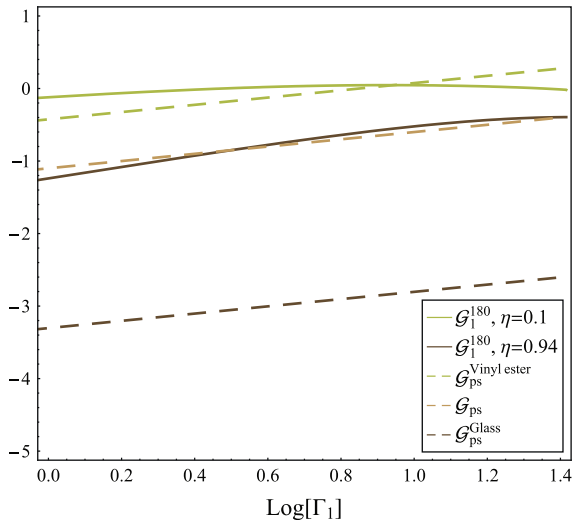

Fig. 11. Comparison between $\mathcal{G}_{ps}$ and $\mathcal{G}_1^{180}$ as functions of Γ_1 in logarithmic scale.

Fig. 11 compares $\mathcal{G}_{ps}$ and $\mathcal{G}_1^{180}$ for a glass-vinyl ester system. In particular, $\mathcal{G}_1^{180}$ is evaluated for two extremely different radius ratios, namely $\eta = 0.1$ and $\eta = 0.94$. $\mathcal{G}_{ps}^{\text{vinyl ester}}$ and $\mathcal{G}_{ps}^{\text{Glass}}$ refer to a penny-shaped crack in vinyl ester resin and glass material, respectively. As shown in Fig. 11, $\mathcal{G}_1^{180}$ presents a non-monotonic behavior for any particle wall thickness as compared to penny-shaped cracks. Therefore, the stable crack growth studied earlier and observed in Fig. 7, can be attributed to cracks' curvature at the particle-matrix interface.

8. Conclusions

Elastic interactions between spherical-cap cracks at the particle-matrix interface of syntactic foams under remote tensile loading are studied in this work. A semi-analytical solution based on an enriched Galerkin method is used to derive stress and displacement fields along the particle-matrix interface including the crack tip vicinity, where singularities and oscillations occur. ERRs for different crack configurations and particle wall thickness are computed and used to understand conditions for stable crack propagation, equal growth, and shielding. Results are specialized to glass-vinyl ester systems used in marine applications.

Analysis shows that crack stability is greatly influenced by the particle wall thickness and configuration of the system of cracks. Small cracks tend to individually grow irrespective of the particle wall thickness. On the other hand, equal crack growth is observed for larger cracks and the critical size for transition is controlled by particle wall thickness. Such growth characteristics are also evinced from representative stress–strain curves that show the occurrence of snap-back instability and softening behaviors. In addition, cracks' shielding is observed irrespective of particle wall thickness. Comparison with an interfacial penny-shaped crack shows that the curvature of particle-matrix interface alters the crack stability.

Acknowledgement

This work is supported by the Office of Naval Research grant N00014-07-1-0419 with Dr. Y. D. S. Rajapakse as the program manager. Views expressed herein are those of authors, and not of the funding agency. The authors thank Nicole Abaid, Matteo Aureli, and Robert Eckhardt for their help in reviewing the manuscript and the Mechanical and Aerospace Engineering Department for the facilities and support provided. The authors would also like to thank the anonymous reviewers for their careful reading of the manuscript and for giving useful suggestions that have helped improve the work and its presentation.

Appendix A

A.1. Lur'e general solutions for displacements and stresses in spherical coordinates

The Navier–Cauchy equation for an isotropic and homogenous body in absence of body forces is

$$(\lambda+\mu)\nabla(\nabla\cdot\mathbf{u})+\mu\Delta\mathbf{u}=\mathbf{0}, \tag{A1}$$

where λ and μ are the Lamé's constants and $\mathbf{u}$ is the displacement vector. By referring to the spherical coordinate system in Fig. 1a and assuming cylindrical symmetry with respect to the y-direction and with respect to the xz-plane, the nonzero components of the displacement and stress fields can be expressed following (Lur'e, 1964) as

$$u_r(r,\theta)=\sum_{n=0}^{\infty}\Big[A_n(n+1)(n-2+4\nu)r^{n+1}+B_n n r^{n-1}+\frac{C_n}{r^n}n(n+3-4\nu)-\frac{D_n(n+1)}{r^{n+2}}\Big]P_n(\cos\theta), \tag{A2a}$$

$$u_\theta(r,\theta)=\sum_{n=1}^{\infty}\Big[A_n(n+5-4\nu)r^{n+1}+B_n r^{n-1}+\frac{C_n}{r^n}(-n+4-4\nu)+\frac{D_n}{r^{n+2}}\Big]\frac{\mathrm{d}P_n(\cos\theta)}{\mathrm{d}\theta}, \tag{A2b}$$

$$\sigma_{rr}(r,\theta)=2\mu\sum_{n=0}^{\infty}\Big[A_n(n+1)(n^2-n-2-2\nu)r^n+B_n n(n-1)r^{n-2}-\frac{nC_n}{r^{n+1}}(n^2+3n-2\nu)+\frac{D_n(n+2)(n+1)}{r^{n+3}}\Big]P_n(\cos\theta), \tag{A2c}$$

$$\tau_{r\theta}(r,\theta)=2\mu\sum_{n=1}^{\infty}\Big[A_n(n^2+2n-1+2\nu)r^n+B_n(n-1)r^{n-2}+\frac{C_n}{r^{n+1}}(n^2-2+2\nu)-\frac{D_n(n+2)}{r^{n+3}}\Big]\frac{\mathrm{d}P_n(\cos\theta)}{\mathrm{d}\theta}, \tag{A2d}$$

$$\sigma_{\theta\theta}(r,\theta)=-2\mu\sum_{n=1}^{\infty}\Big\{\Big[A_n(n^2+4n+2+2\nu)(n+1)r^n+n^2B_nr^{n-2}-\frac{C_n}{r^{n+1}}n(n^2-2n-1+2\nu)+\frac{D_n(n+1)^2}{r^{n+3}}\Big]P_n(\cos\theta)-\Big[A_n(n+5-4\nu)r^n+B_nr^{n-2}+\frac{C_n}{r^{n+1}}(-n+4-4\nu)+\frac{D_n}{r^{n+3}}\Big]\times\frac{\mathrm{d}P_n(\cos\theta)}{\mathrm{d}\theta}\cot\theta\Big\}. \tag{A2e}$$

Here, A_n, B_n, C_n, and D_n are unknown coefficients, ν is the Poisson's coefficient, and $P_n(\cos\theta)$ is the nth Legendre polynomial in $\cos\theta$. Further note that the Lame's coefficients can be written in terms of ν and the Young's modulus E. Legendre polynomials and their derivatives are orthogonal with respect to θ in the range $[0,\pi]$. In addition,

$$\int_0^{\pi}P_n(\cos\theta)P_n(\cos\theta)\sin\theta\mathrm{d}\theta=\frac{2}{2n+1}, \tag{A3a}$$

$$\int_0^{\pi}\frac{\mathrm{d}P_n(\cos\theta)}{\mathrm{d}\theta}\frac{\mathrm{d}P_n(\cos\theta)}{\mathrm{d}\theta}\sin\theta\mathrm{d}\theta=\frac{2n(n+1)}{2n+1}. \tag{A3b}$$

A.2. Solutions of subproblems (I) and (II)

Subproblem (I) is symmetric with respect to the equatorial plane of the spherical void for any value α_1 and α_2. The external load can be expressed in polar coordinate following (Lur'e, 1964) as

$$\bar{\sigma}_{rr}(\theta)=\frac{\sigma_\infty}{3}[1+2P_2(\cos\theta)], \tag{A4a}$$

$$\bar{\tau}_{r\theta}(\theta)=\frac{\sigma_\infty}{3}\frac{\mathrm{d}P_2(\cos\theta)}{\mathrm{d}\theta}. \tag{A4b}$$

Thus, the solution of subproblem (I) is written by using the first two even terms of the series in Eqs. (A2a) and (A2b) as follows

$$\frac{2\mu_m}{a\sigma_\infty}u_r^{(\mathrm{I})}(a,\theta)=\frac{3(\nu_m-1)[4+5(\nu_m+1)]\cos(2\theta)}{2(5\nu_m^2-2\nu_m-7)}, \tag{A5a}$$

$$\frac{2\mu_m}{a\sigma_\infty}u_\theta^{(\mathrm{I})}(a,\theta)=\frac{15(\nu_m-1)\sin(2\theta)}{2(5\nu_m-7)}. \tag{A5b}$$

Subproblem (II) is generally referred to as external (Lur'e, 1964). Since stress and displacement fields vanish as $r\to\infty$, the constants A_n and B_n in equation set (A2e) are zero. Thus, solution of subproblem II is obtained from equation set (A2e) by specializing the elastic constants to the matrix material, applying the suitable boundary conditions, and solving for C_n and D_n. After manipulation, the displacement fields at $r=a$ are

$$\frac{2\mu_m}{a\sigma_\infty}u_r^{(\mathrm{II})}(a,\theta)=\sum_{n=0}^{\infty}\frac{\mathsf{A}_n^{(r\sigma)}\sigma_n+\mathsf{A}_n^{(r\tau)}\tau_n}{\mathsf{B}_n^{(r)}}P_n(\cos\theta), \tag{A6a}$$

$$\frac{2\mu_m}{a\sigma_\infty}u_\theta^{(\mathrm{II})}(a,\theta)=\sum_{n=1}^{\infty}\frac{\mathsf{A}_n^{(\theta\sigma)}\sigma_n+\mathsf{A}_n^{(\theta\tau)}\tau_n}{\mathsf{B}_n^{(\theta)}}\frac{\mathrm{d}P_n(\cos\theta)}{\mathrm{d}\theta}, \tag{A6b}$$

where the expressions for the coefficients $\mathsf{A}_n^{(r\sigma)}$, $\mathsf{A}_n^{(r\tau)}$, $\mathsf{B}_n^{(r)}$, $\mathsf{A}_n^{(\theta\sigma)}$, $\mathsf{A}_n^{(\theta\tau)}$, and $\mathsf{B}_n^{(\theta)}$ are reported in equation set (A5) of (Tagliavia et al., 2010b).

A.3. Matrix form of the linear system in equation set (13b)

The matrix $\mathbf{F}$ is a square matrix composed of four $(d+2)\times(d+2)$ as

$$\mathbf{F}=\int_{\alpha_1}^{\alpha_2}\int_{\alpha_1}^{\alpha_2}\begin{pmatrix}\mathbf{R}_{\sigma\sigma} & \mathbf{R}_{\sigma\tau}\\ \mathbf{C}_{\tau\sigma} & \mathbf{C}_{\tau\tau}\end{pmatrix}\mathrm{d}\theta\mathrm{d}\hat{\theta}, \tag{A7}$$

where each block can be written as

$$\mathbf{R}_{ij}=\begin{pmatrix}\mathcal{F}^{(\eta\jmath)}(\theta,\hat{\theta})\rho_0^{(i)}(\theta)\rho_0^{(j)}(\hat{\theta}) & \cdots & \mathcal{F}^{(\eta\jmath)}(\theta,\hat{\theta})\rho_0^{(i)}(\theta)\rho_{d+1}^{(j)}(\hat{\theta})\\ \vdots & \ddots & \vdots\\ \mathcal{F}^{(\eta\jmath)}(\theta,\hat{\theta})\rho_{d+1}^{(i)}(\theta)\rho_0^{(j)}(\hat{\theta}) & \cdots & \mathcal{F}^{(\eta\jmath)}(\theta,\hat{\theta})\rho_{d+1}^{(i)}(\theta)\rho_{d+1}^{(j)}(\hat{\theta})\end{pmatrix}, \tag{A8a}$$

$$\mathbf{C}_{ij}=\begin{pmatrix}\mathcal{F}^{(\theta\jmath)}(\theta,\hat{\theta})\rho_0^{(i)}(\theta)\rho_0^{(j)}(\hat{\theta}) & \cdots & \mathcal{F}^{(\theta\jmath)}(\theta,\hat{\theta})\rho_0^{(i)}(\theta)\rho_{d+1}^{(j)}(\hat{\theta})\\ \vdots & \ddots & \vdots\\ \mathcal{F}^{(\theta\jmath)}(\theta,\hat{\theta})\rho_{d+1}^{(i)}(\theta)\rho_0^{(j)}(\hat{\theta}) & \cdots & \mathcal{F}^{(\theta\jmath)}(\theta,\hat{\theta})\rho_{d+1}^{(i)}(\theta)\rho_{d+1}^{(j)}(\hat{\theta})\end{pmatrix}. \tag{A8b}$$

All the others terms in Eqs. (14) and (15) are obtained by manipulating equation set (13b), thus can be written as follows

$$\boldsymbol{\omega} = \left(\omega_0^{(\sigma)}, \quad \omega_1^{(\sigma)}, \quad \cdots, \quad \omega_{d+1}^{(\sigma)}, \quad \omega_0^{(\tau)}, \quad \omega_1^{(\tau)}, \quad \cdots, \quad \omega_{d+1}^{(\tau)} \right)^{\mathrm{T}}, \tag{A9a}$$

$$\chi_r(\theta, B_1) = -\frac{2\mu_m}{a}\left[\frac{u_r^{(\mathrm{I})}(a,\theta)}{\sigma_\infty} - B_1 \cos\theta\right], \tag{A9b}$$

$$\chi_\theta(\theta, B_1) = -\frac{2\mu_m}{a}\left[\frac{u_\theta^{(\mathrm{I})}(a,\theta)}{\sigma_\infty} + B_1 \sin\theta\right], \tag{A9c}$$

$$\boldsymbol{\chi}(B_1) = \int_{\alpha_1}^{\alpha_2} \left(\chi_r(\theta, B_1)\rho_0^{(\sigma)}(\theta), \quad \cdots, \quad \chi_r(\theta, B_1)\rho_{d+1}^{(\sigma)}(\theta), \quad \chi_\theta(\theta, B_1)\rho_0^{(\tau)}(\theta), \quad \cdots, \quad \chi_\theta(\theta, B_1)\rho_{d+1}^{(\tau)}(\theta) \right)^{\mathrm{T}} \mathrm{d}\theta, \tag{A9d}$$

$$\boldsymbol{\kappa} = \int_{\alpha_1}^{\alpha_2} \left(\cos\theta \sin\theta \rho_0^{(\sigma)}(\theta), \quad \cdots, \quad \cos\theta \sin\theta \rho_{d+1}^{(\sigma)}(\theta), \quad -\sin^2\theta \rho_0^{(\tau)}(\theta), \quad \cdots, \quad -\sin^2\theta \rho_{d+1}^{(\tau)}(\theta) \right)^{\mathrm{T}} \mathrm{d}\theta. \tag{A9e}$$

Note that in Eq. (A9e) the definition of $P_1(\cos\theta)$ is used.

References

Abramowitz, M., Stegun, I.A., 1965. Handbook of Mathematical Functions. Dover, New York, NY.

Andrews, M.G., Massabò, R., 2007. The effects of shear and near tip deformations on energy release rate and mode mixity of edge-cracked orthotropic layers. Engineering Fracture Mechanics 74 (17), 2700–2720.

Andrews, M.G., Massabò, R., 2008. Delamination in flat sheet geometries with material imperfections and thickness variations. Composites Part B: Engineering 39 (1), 139–150.

Andrews, M.G., Massabò, R., Cox, B.N., 2006. Elastic interaction of multiple delaminations in plates subject to cylindrical bending. International Journal of Solids and Structures 43 (5), 855–886.

Ayhan, A.O., Kaya, A.C., Nied, H.F., 2006. Analysis of three-dimensional interface cracks using enriched finite elements. International Journal of Fracture 142 (3–4), 255–276.

Babolian, E., Delves, L.M., 1979. An augmented Galerkin method for first kind Fredholm equations. Journal of Applied Mathematics 24 (2), 157–174.

Bardella, L., Genna, F., 2001a. Elastic design of syntactic foamed sandwiches obtained by filling of three-dimensional sandwich-fabric panels. International Journal of Solids and Structures 38 (2), 307–333.

Bardella, L., Genna, F., 2001b. On the elastic behavior of syntactic foams. International Journal of Solids and Structures 38 (40–41), 7235–7260.

Barpi, F., Valente, S., 1998. Size-effects induced bifurcation phenomena during multiple cohesive crack propagation. International Journal of Solids and Structures 35 (16), 1851–1861.

Bazant, Z.P., Planas, J., 1998. Fracture and Size Effect in Concrete and Other Quasibrittle Materials. CRC Press, Boca Raton, FL.

Bazant, Z.P., Tabbara, M.R., 1992. Bifurcation and stability of structures with interacting propagating cracks. International Journal of Fracture 53 (3), 273–289.

Benabou, L., Benseddiq, N., Nat-Abdelaziz, M., 2005. The energy release rate of a crack in the interfacial zone of particulate-reinforced composites. Mechanics of Materials 37 (5), 551–563.

Carpinteri, A., Monetto, I., 1999. Snap-back analysis of fracture evolution in multi-cracked solids using boundary element method. International Journal of Fracture 98 (3), 225–241.

Ching, H.-K., Batra, R.C., 2001. Determination of crack tip fields in linear elastostatics by the meshless local Petrov–Galerkin (MLPG) method. Computer Modeling in Engineering & Sciences 2 (2), 273–289.

Chiu, T.C., Lin, H.C., 2009. Analysis of stress intensity factors for three-dimensional interface crack problems in electronic packages using the virtual crack closure technique. International Journal of Fracture 156 (1), 75–96.

Cho, J., Joshi, M.S., Sun, C.T., 2006. Effect of inclusion size on mechanical properties of polymeric composites with micro and nano particles. Composites Science and Technology 66 (13), 1941–1952.

Christensen, R.M., 1979. Mechanics of Composite Materials. Dover, Mineola, NY.

Dundurs, J., 1969. Discussion of a paper by D.B. Bogy. Journal of Applied Mechanics 36, 650–652.

Fleming, M., Chu, Y.A., Moran, B., Belytschko, T., 1997. Enriched element-free Galerkin methods for crack tip fields. International Journal for Numerical Methods in Engineering 40 (8), 1483–1504.

Gdoutos, E.E., 2005. Fracture Mechanics: An Introduction. Springer, Norwell, MA.

Gladysz, G.M., Perry, B., Mceachen, G., Lula, J., 2006. Three-phase syntactic foams: structure-property relationships. Journal of Materials Science 41 (13), 4085–4092.

Gorbatikh, L., 2004. On elastic compliances of interfacial cracks. International Journal of Fracture 127 (2), L141–L148.

Gosz, M., Dolbow, J., Moran, B., 1998. Domain integral formulation for stress intensity factor computation along curved three-dimensional interface cracks. International Journal of Solids and Structures 35 (15), 1763–1783.

Griffith, A.A., 1921. The phenomena of rupture and flow in solids. Philosophical Transactions of the Royal Society of London. Series A, Containing Papers of a Mathematical or Physical Character 221, 163–198.

Guo, C., Sun, C.T., 1997. Dynamic Mode-I crack-propagation in a carbon/epoxy composite. Composites Science and Technology 58 (9), 1405–1410.

Gupta, N., Ye, R., Porfiri, M., 2010. Comparison of tensile and compressive characteristics of vinyl ester/glass microballoon syntactic foams. Composites Part B: Engineering 41 (3), 236–245.

Hamoush, S.A., Ahmad, S.H., 1989. Fracture energy release rate of adhesive joints. International Journal of Adhesion and Adhesives 9 (3), 171–178.

Huang, J.H., 1995. An ellipsoidal inclusion or crack in orthotropic piezoelectric media. Journal of Applied Physics 78 (11), 6491–6503.

Huang, J.S., Gibson, L.J., 1993. Elastic moduli of a composite of hollow spheres in a matrix. Journal of the Mechanics and Physics of Solids 41 (1), 55–75.

Hwang, C.G., Ingraffea, A.R., 2004. Shape prediction and stability analysis of Mode-I planar cracks. Engineering Fracture Mechanics 71 (12), 1751–1777.

Islam, M.M., Kim, H.S., 2007. Novel syntactic foams made of ceramic hollow microspheres and starch: theory, structure and properties. Journal of Materials Science 42 (15), 6123–6132.

John, B., Nair, C.P.R., Devi, K.A., Ninan, K.N., 2007. Effect of low-density filler on mechanical properties of syntactic foams of cyanate ester. Journal of Materials Science 42 (14), 5398–5405.

Kassir, M.K., Bregman, A.M., 1972. The stress-intensity factor for a penny-shaped crack between two dissimilar materials. Journal of Applied Mechanics 39, 308–310.

Kilic, B., Madenci, E., 2007. Hypersingular integral equations for the solution of penny-shaped interface crack problems. Journal of Mechanics of Materials and Structures 2 (4), 729–751.

Kim, H.S., Plubrai, P., 2004. Manufacturing and failure mechanisms of syntactic foam under compression. Composites Part A: Applied Science and Manufacturing 35 (9), 1009–1015.

Kinloch, A., Mohammed, R., Taylor, A., Eger, C., Sprenger, S., Egan, D., 2005. The effect of silica nano particles and rubber particles on the toughness of multiphase thermosetting epoxy polymers. Journal of Materials Science 40 (18), 5083–5086.

Kishore, Shankar, R., Sankaran, S., 2005. Gradient syntactic foams: tensile strength, modulus and fractographic features. Materials Science and Engineering: A 412 (1-2), 153–158.

Koopman, M., Chawla, K.K., Carlisle, K.B., Gladysz, G.M., 2006. Microstructural failure modes in three-phase glass syntactic foams. Journal of Materials Science 41 (13), 4009–4014.

Kuang, J.S., Wang, Y.H., 1999. Analysis of interfacial cracks emanating from a hole in a bi-material plate. European Journal of Mechanics - A/Solids 18 (3), 465–479.

Lee, J., Yee, A.F., 2001. Fracture behavior of glass bead filled epoxies: cleaning process of glass beads. Journal of Applied Polymer Science 79 (8), 1371–1383.

Lee, W., Howard, S.J., Clegg, W.J., 1996. Growth of interface defects and its effect on crack deflection and toughening criteria. Acta Materialia 44 (10), 3905–3922.

Lur'e, A.I., 1964. Three-Dimensional Problems of the Theory of Elasticity. Interscience, New York, NY.

Marotzke, C., Qiao, L., 1997. Interfacial crack propagation arising in single-fiber pull-out tests. Composites Science and Technology 57 (8), 887–897.

Martynenko, M.A., Lebedyeva, I.V., 2006. Axisymmetric problem for a spherical crack on the interface of elastic media. Journal of Engineering Mathematics 56 (4), 371–384.

Marur, P.R., 2005. Effective elastic moduli of syntactic foams. Materials Letters 59 (14-15), 1954–1957.

Marur, P.R., 2009. Influence of imperfect interface on the elastic moduli of syntactic foams. Computational Materials Science 46 (2), 327–332.

Narkis, M., Kenig, S., Puterman, M., 1984. Three-phase syntactic foams. Polymer Composites 5 (2), 159–165.

Nemat-Nasser, S., 1978. Stability of a system of interacting cracks. International Journal of Engineering Science 16 (4), 277–285.

Pawlak, A., Galeski, A., 2002. Determination of stresses around beads in stressed epoxy resin by photoelasticity. Journal of Applied Polymer Science 86 (6), 1436–1444.

Porfiri, M., Gupta, N., 2009. Effect of volume fraction and wall-thickness on the elastic properties of hollow-particle filled composites. Composites Part B: Engineering 40 (2), 166–173.

Prasad, P.B.N., Simha, K.R.Y., 2002. Interactions of interfacial arc cracks. International Journal of Fracture 117 (1), 39–62.

Rice, J.R., 1988. Elastic fracture-mechanics concepts for interfacial cracks. Journal of Applied Mechanics 55 (1), 98–103.
Rohatgi, P.K., Gupta, N., Alaraj, S., 2006. Thermal expansion of aluminum-fly ash cenosphere composites synthesized by pressure infiltration technique. Journal of Composite Materials 40 (13), 1163–1174.
Saleh, A.L., Aliabadi, M.H., 1995. Crack growth analysis in concrete using boundary element method. Engineering Fracture Mechanics 51 (4), 533–545.
Sauvant-Moynot, V., Gimenez, N., Sautereau, H., 2006. Hydrolytic ageing of syntactic foams for thermal insulation in deep water: degradation mechanisms and water uptake model. Journal of Materials Science 41 (13), 4047–4054.
Singh, I.V., Mishra, B.K., Pant, M., 2010. A modified intrinsic enriched element free Galerkin method for multiple cracks simulation. Materials & Design 31 (1), 628–632.
Sneddon, I.N., 1979. The stress intensity factor for a flat elliptical crack in an elastic solid under uniform tension. International Journal of Engineering Science 17 (2), 185–191.
Sumi, Y., Nemat-Nasser, S., Keer, L.M., 1980. A new combined analytical and finite-element solution method for stability analysis of the growth of interacting tension cracks in brittle solids. International Journal of Engineering Science 18 (1), 211–224.
Suo, X.Z., Combescure, A., 1992. Second variation of energy and an associated line independent integral in fracture mechanics. I. Theory. European Journal of Mechanics - A/Solids 11 (5), 609–624.
Suo, X.Z., Valeta, M.P., 1998. Second variation of energy and an associated line independent integral in fracture mechanics. II. Numerical validations. European Journal of Mechanics - A/Solids 17 (4), 541–565.
Tagliavia, G., Porfiri, M., Gupta, N., 2010a. Analysis of flexural properties of hollow-particle filled composites. Composites Part B: Engineering 41 (1), 86–93.
Tagliavia, G., Porfiri, M., Gupta, N., 2010b. Analysis of hollow inclusion-matrix debonding in particulate composites. International Journal of Solids and Structures 47 (16), 2164–2177.
Taya, M., 1981. On stiffness and strength of an aligned short-fiber reinforced composite containing penny-shaped cracks in the matrix. Journal of Composite Materials 15 (3), 198–210.
Wouterson, E.M., Boey, F.Y.C., Hu, X., Wong, S.C., 2005. Specific properties and fracture toughness of syntactic foam: effect of foam microstructures. Composites Science and Technology 65 (11-12), 1840–1850.